SolarCell INSIGHTS

dev.solarcellinsights.com

Research Article

test 3

pudo mia*

Cite This: https://doi.org/10.5555/sci.14

Read Online

OPEN ACCESS | HTML version | Cite & DOI | Licence CC BY 4.0

ABSTRACT: sf

KEYWORDS: *"degradation study*

Received 30 September 2026 **Accepted** 17 October 2026 **Published** 24 October 2026 **Vol. 1 No. 1 (2026): Test 1st issue**

INTRODUCTION

In recent years, significant advancements have been made in the design of organic semiconductor materials, the modification of thin-film microstructures, and the optimization of devices using novel charge-carrier transport materials. These developments together have led to a boost in the power conversion efficiency (PCE) of organic solar cells (OSCs), today surpassing the 19% threshold [1-8]. The significant attention garnered by OSCs can be attributed to their potential for high-throughput processing/manufacturing, lightweight, semi-transparent, and flexible devices, as well as impressive form factors. These attributes make organic photovoltaics a promising technology to contribute to the global energy transition by offering affordable and environmentally friendly (green) electricity, using also non-toxic photoactive materials [9-16]. Improving the stability of OSCs is a critical factor that must be achieved to eventually ensure their widescale application and successful commercialization [17-22]. The observed operational lifetimes of state-of-the-art high-performance OSCs, which are currently measured in the range of hundreds of hours, have been deemed inadequate [23], in the realm of practical application. Under real-world operating conditions, extrinsic stressors, such as oxygen, moisture, temperature, and radiation, significantly affect stability and accelerate the degradation of OSCs [24-28].

The active layer morphology undergoes undesired morphological changes, while the charge carrier transport layers and electrode materials can diffuse into the photoactive layer, even in the absence of external stressors [29]. The permeation of ambient oxygen and water into a device can cause chemical and physical degradation, causing deterioration of the electrodes, interlayers, and photoactive layers [30-33]. Furthermore, the operational stability of OSCs is inherently affected by light-induced degradation, as these devices rely on light to function. Light-induced degradation introduces a significant limitation to the long-term stability of OSCs, as it accelerates degradation processes within the device [28, 34].

Thermal stress, particularly at elevated temperatures, leads to spinodal demixing of the bulk-heterojunction (BHJ) photoactive layer. However, component demixing can also occur at ambient temperature, due to the non-equilibrium (frozen) morphology of the BHJs [35]. Recent studies of thermally induced degradation and photo-degradation processes provided a deeper understanding of the underlying mechanisms involved [29, 36-40]. Under continuous illumination, OSCs typically exhibit a rapid decline in efficiency over a relatively short time, commonly referred to as "burn-in." Subsequently, a more gradual and steadier decrease in efficiency occurs over an extended period of time [41-44].

The performance of OSCs is governed by the energetic landscape and nanoscale morphology of the BHJ materials [45, 46]. These factors crucially influence device processes, including charge transfer and separation, carrier transport within the device, and carrier collection from the photoactive layer. Optimized blend morphologies, as observed in various studies, exhibit a certain sensitivity to temperature-induced ageing, arising from the tendency of the photoactive layer morphology to evolve towards a thermodynamically stable state [47]. Consequently, this evolution can result in significant component demixing, leading to a reduction in the overall interfacial area between the donor and acceptor components (commonly referred to as the D-A interfacial area or heterojunction), adversely affecting device performance [48, 49].

For fullerene-based organic solar cells, extensive photo-thermal studies have been performed in the past few decades [50]. For non-fullerene acceptor (NFA)-based devices, on the other hand, stability research is currently in its nascent stage [51-54]. Numerous NFA-based OSCs exhibit remarkable efficiency; however, their poor thermal stability is a key obstacle hampering practical applications [55].

In the realm of photovoltaic devices, suboptimal morphologies and processes can significantly reduce overall device performance [56], resulting in loss processes, such as increased charge recombination. Therefore, understanding the loss mechanisms and judicious control of the BHJ morphology is critical to overcoming the existing limitations [57-59]. Until today, there have been a few reports on the impact of thermal annealing on component demixing in the photoactive layer, as well as its effect on the transport layers and electrode interfaces. Importantly, thermal annealing is necessary to discharge water and oxygen after the transport layer is deposited, but it also causes structural and morphological

© 2026 The authors · CC BY 4.0

changes that may adversely affect device performance. Additionally, a detailed understanding of the energetics of D-A mixtures after thermal annealing is also missing.

X-ray scattering techniques such as grazing incidence wide-angle X-ray scattering (GIWAXS) have been widely used to examine bulk morphology quantitatively, providing insights into crystallinity and crystal orientation. Additionally, resonant soft X-ray scattering (RSoXS) measures interface roughness, domain size, and purity [60]. On the other hand, atomic force microscopy (AFM) is commonly used to investigate the surface topography, which can also provide insight into the bulk morphology [61, 62]. Regrettably, these approaches examine phase separation only at a nanoscale level within very limited spatial regions. Steady-state optical microscopy techniques, on the other hand, including absorbance and photoluminescence studies, enable a qualitative understanding of polymer order and domain size over a larger area. These methods allow for averaging across broad regions, but do not provide high local resolution. Optical imaging can be used to examine morphological variations or alterations across extensive areas; however, comprehensive information on the material characteristics is generally lacking. Given the direct correlation between the electronic characteristics (charge transfer and separation, recombination, and extraction) of the photoactive layer and its morphology, spatially resolved optoelectronic measuring techniques can be leveraged to discern film morphology indirectly. Based on these spatially resolved optoelectronic measurements, it is possible to derive localized electrical characteristics, including the dark saturation current and series resistance of the photoactive layer. To examine the macroscopic differences in morphology across larger-area devices, it is possible to use imaging techniques such as photoluminescence imaging (PLI), electroluminescence imaging (ELI), and scanning techniques like light-beam induced current (LBIC) measurements [63-66]. Previous research studies have examined morphology and phase separation through these high-resolution imaging techniques, focusing on the device's limited area of interest. However, a significant amount of phase separation often exhibits vertical concentration gradients between the original phases [22, 56].

In this work, we present a comprehensive study of large-scale phase separation across the entire active area of the sample, leveraging a number of imaging and scanning techniques. As a result, we determine the necessary conditions for achieving highly efficient bulk heterojunction (BHJ) geometries. More specifically, we aim to examine the impact of thermal degradation on state-of-the-art OSCs based on PM6:Y6 by subjecting them to different annealing temperatures in a nitrogen atmosphere. The factors contributing to the corrosion of the device can be attributed to morphological changes occurring within the photoactive layer. The device, in its as-cast state, demonstrates a short-circuit current density (J_{SC}) of 23.26 mA.cm^{-2}, an open-circuit voltage (V_{OC}) of 848 mV, and a fill factor (FF) of 59%, yielding a PCE of 11.64%. While an initial performance improvement is seen upon thermal annealing at 80 °C, subsequently, a significant decline of V_{OC}, FF, and PCE is observed, whereas the J_{SC} remained virtually constant.

RESULTS AND DISCUSSION

2.1. Photovoltaic properties

Figure 1a and **1b** depict the chemical structures and the device layer stack. Using an inverted device architecture, BHJ OSC devices have been fabricated with PM6:Y6 as the photoactive layer. The device structure consisted of glass/ITO/ZnO/PM6:Y6/MoO_3/Ag. Additional information regarding device preparation can be found in the experimental section. After device fabrication, thermal annealing was performed on the devices for 10 min at various temperatures using a hotplate in a nitrogen-filled glovebox, with non-annealed devices serving as a reference. The annealing experiments were deliberately conducted in a nitrogen atmosphere to separate thermal effects on morphology and device performance from other degradation channels. While this approach excludes oxygen- and moisture-induced degradation, it enables a clear interpretation of the thermally driven processes.

Figures 1c and **1d** show the J-V characteristics under simulated one-sun illumination and the EQEs of devices after annealing at different temperatures. The dark J-V characteristics are presented in Supporting Information (**SI**). The reference device in its as-cast state exhibited diode-like characteristics, with a rectification ratio exceeding two orders of magnitude when comparing the current density under reverse and forward bias. This is shown in **Figure S1** in the **SI**.

The photovoltaic parameters reveal that device performance is highly sensitive to annealing temperature. The J_{SC} increased as the post-processing annealing temperature increased up to 140 °C; thereafter, the J_{SC} was nearly constant (**Table 1**). The J_{SC} observed from devices exposed to elevated annealing temperatures indicates that the thermal treatment did not impact absorption and exciton generation in PM6:Y6. In fact, the EQE spectra confirm that the absorption coefficient and spectral response are preserved, suggesting that the morphological changes induced by crystallization and phase separation primarily impact charge extraction rather than charge generation. Moderate annealing (80 °C – 110 °C) yields stable J_{SC} and V_{OC}, while maintaining relatively high FF, reflecting a balanced charge generation and extraction process. Beyond 140 °C, V_{OC} begins to decline, and FF drops significantly, particularly at temperatures between 170 °C and 200 °C, indicating increased non-radiative recombination. These trends confirm an optimum thermal window of around 80 °C to 140 °C, while excessive annealing accelerates morphological and electrical degradation, resulting in reduced efficiency. These trends confirm an optimum thermal window of around 80 °C to 140 °C, while excessive annealing accelerates morphological and electrical degradation, resulting in reduced efficiency. The statistical analysis of several photovoltaic parameters for different annealing temperatures can be found in **Figure S2**.

Table 1: Photovoltaic parameters corresponding to the OSCs as-cast annealed at varying temperatures (EQE corrected). Here, the short-circuit current is J_{SC}, the open-circuit voltage is V_{OC}, the fill factor is FF, the power conversion efficiency is η, the series resistance is R_S, and the parallel resistance is R_P. The samples were annealed at different temperatures for 10 min.

© 2026 The authors · CC BY 4.0

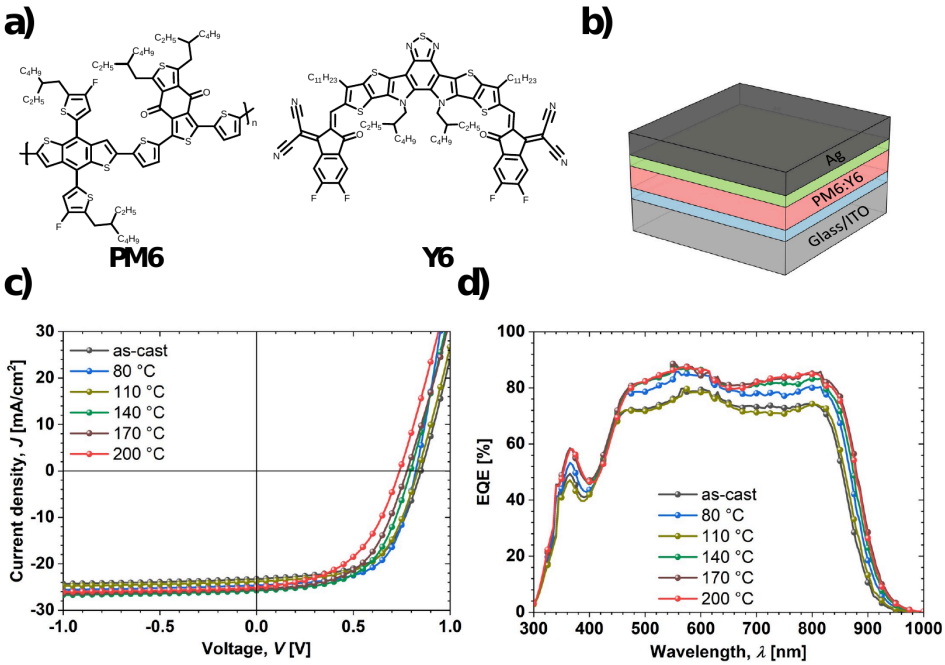

Figure 1: **(a)** Schematic representation of the chemical structures of PM6 and Y6, **(b)** depiction of the inverted polymer solar cell architecture, **(c)** current density-voltage (J-V) characteristics, **(d)** external quantum efficiency (EQE) measurements of the PM6:Y6 OSCs as-cast and upon annealing at different temperatures.

Annealing temperature	J_{SC} (mA/cm²)	J_{SC} (EQE) (mA/cm²)	V_{OC} (mV)	FF (%)	η (%)	Rs (Ω)	Rp (Ω)
As-cast	23.26	22.74	848	59	11.64	8	1237
80 °C	**24.64**	**24.85**	**821**	**62**	**12.55**	**6**	**1370**
110 °C	23.77	22.72	832	59	11.72	7	1338
140 °C	25.76	25.83	795	57	11.63	7	1205
170 °C	25.39	26.45	777	55	10.86	7	1207
200 °C	25.00	26.21	738	50	9.26	10	734

2.2. Photoluminescence imaging (PLI)

Photoluminescence imaging (PLI) is a non-destructive, all-optical technique that sheds light on OSCs' opto-electronic properties and film quality. In PLI, the photoactive layer within the device stack can absorb light and subsequently emit photoluminescence, providing insight into charge carrier recombination, the quality of the thin film, and device performance. This highly sensitive imaging technique allowed us to visualize the spatial distribution of photogenerated charge carriers, defects, and non-uniformities. It can be used to make improvements both in material design and device fabrication.

Figure 2 shows the PLI of PM6:Y6 devices measured under 470 nm diode excitation after annealing. The as-cast device exhibited the highest PL intensity, while the PL intensity gradually decreased with increasing annealing temperature. Thermal annealing can cause changes in the charge carrier recombination occurring in the device, for example, by variation of the trap state distribution.

However, in OSCs, photoluminescence effectively probes exciton quenching, which is controlled by the magnitude of component demixing (often called phase separation). The observed reduction in PL intensity over the whole device area thus indicates a more intimate mixing, leaving fewer excitons unquenched as they can more easily reach the donor-acceptor interface. These results suggest that the reduction in PLI intensity arises from a complex interplay between improved donor–acceptor mixing and thermally induced loss channels, which evolve differently across the annealing range.

2.3. Electroluminescence imaging (ELI)

Electroluminescence imaging (ELI) is a technique used to study OSCs, and organic light-emitting diodes (OLEDs) based on the detection of the device´s local electroluminescence. In the context of OSCs, ELI enables the spatial mapping of electroluminescence across the surface of the OSC, providing valuable insights into the spatial distribution of charge carriers, recombination processes, and overall device efficiency. According to the reciprocity theorem, a solar cell's external electroluminescence quantum efficiency EL_{QE} observed under forward bias (carrier injection) corresponds to a higher EQE under illumination [67]. Furthermore, ELI can help to optimize device fabrication processes by revealing areas of non-uniformity and defects.

© 2026 The authors · CC BY 4.0

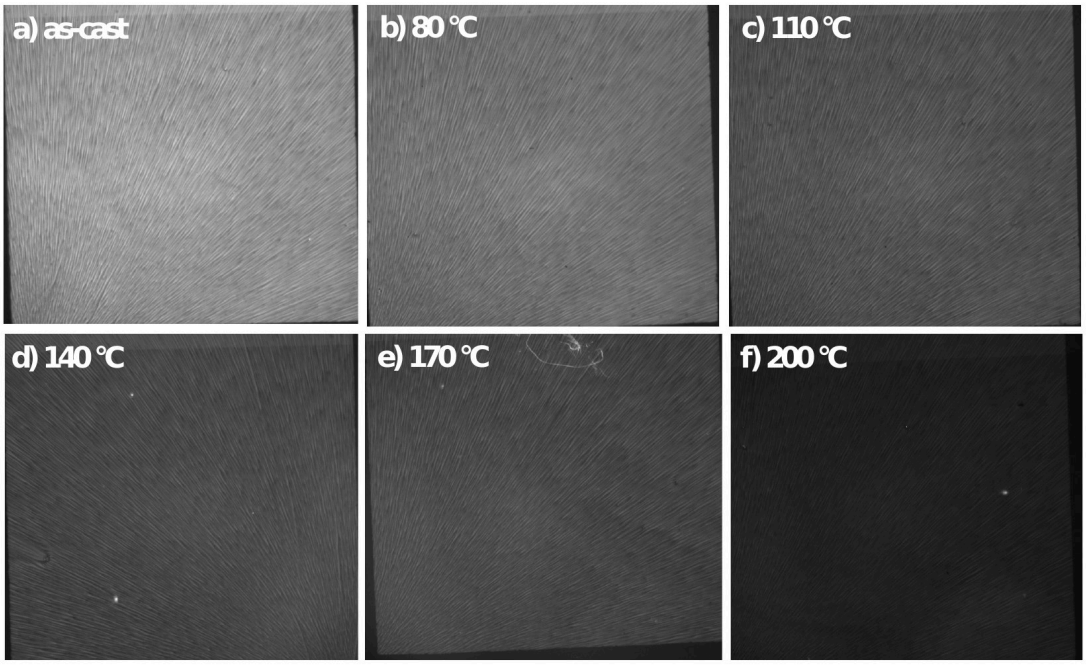

Figure 2: Photoluminescence imaging (PLI) of PM6:Y6 devices. Each sub-image is a response to the actual cell size of 7 × 6 mm². (a) as-cast, (b) 80 °C, (c) 110 °C, (d) 140 °C, (e) 170 °C, and (f) 200 °C. All measurements were taken under the same excitation conditions, and the intensities are comparable.

ELI is performed on devices after annealing at different temperatures to investigate the mechanisms of charge carrier injection and their recombination within the photoactive layer (see **Figure 3**). According to the reciprocity theorem, the charge injection process is intimately linked to charge extraction *via* the hole and electron transport layers. It is important to note that temperature changes can significantly influence the barrier for charge injection when the transport layers undergo changes. Upon thermal annealing up to 110 °C, no significant changes can be observed in the EL intensity; however, the EL intensity is reduced for the devices annealed at higher temperatures. An apparent stripe-type pattern is visible in all EL images of the devices, similar to the PL images. In the case of the device annealed at elevated temperature, the reduction in ELI intensity can be attributed to temperature-dependent modifications in charge-injection barriers and the appearance of interfacial defects or partially degraded sealing layers, which reduce radiative recombination efficiency under electrical excitation. This stripe pattern is a common side effect of spin coating, sometimes called the spin-coating star, mainly when chloroform is used as a solvent.

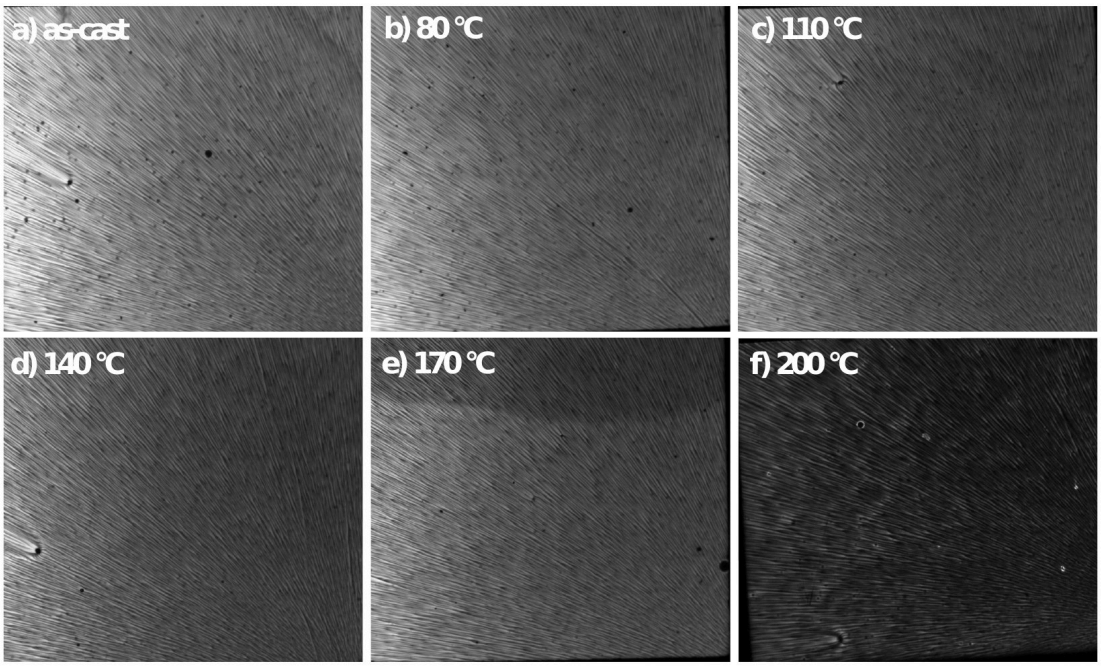

Figure 3: Electroluminescence imaging (ELI) of PM6:Y6 devices measured by applying the current. Each sub-image is a response to the actual cell size of 7 x 6 mm². (a) as-cast, (b) 80 °C, (c) 110 °C, (d) 140 °C, (e) 170 °C, and (f) 200 °C.

© 2026 The authors · CC BY 4.0

The evolution of both PLI and ELI intensities can be understood in terms of the balance between exciton dissociation (charge generation) and non-radiative recombination. At moderate annealing temperatures (≤ 140 °C), the slight reduction in PLI intensity reflects enhanced exciton quenching at the donor–acceptor interface, consistent with more intimate nanoscale mixing, facilitating charge separation. However, further temperature increase induces PM6 crystallization and vertical phase separation, which diminishes the interfacial area and introduces energetic disorder and trap states. These structural changes increase non-radiative recombination losses, manifested in a pronounced decrease in PLI and ELI intensities. Thus, the evolution of luminescence with temperature indicates a transition from morphology-driven enhanced exciton dissociation to thermally induced degradation, resulting in non-radiative recombination pathways [68-70]. The simultaneous reduction in PL and EL intensities (**Figures S3–S6**) with increasing annealing temperature, accompanied by the decline in Voc, indicates non-radiative recombination pathways. These losses likely originate from trap states and increased energetic disorder introduced by crystallization and demixing, as evidenced by AFM and GIWAXS analyses. Such structural rearrangements reduce the interfacial area and promote exciton quenching via non-radiative decay.

2.4. Light Beam-Induced Current (LBIC)

To gain insight into the spatial distribution of photocurrent generation within the device, light-beam-induced current (LBIC) measurements are performed. LBIC uses a focused light beam, typically a laser light source, to selectively illuminate different regions of a device's surface. As the focused light beam (typically between 5 and 20 µm in diameter) is scanned across the device surface, the resulting local photocurrent is measured, providing a spatial map of the photocurrent distribution. This spatial mapping allows for identifying variations in efficiency, defects, and non-uniformities across the device.

Figure 4 shows the LBIC measurements of PM6:Y6-based solar cells annealed at different temperatures. Although the current flows uniformly through the as-cast device, the spatial current distribution becomes less uniform for higher annealing temperatures. This observation may indicate changes in the charge transport layers, considering that the EQE data show the highest photocurrents for even the highest annealing temperatures. It should be noted that LBIC provides local photocurrent mapping, while EQE represents an area-averaged response. The reduced uniformity observed in the LBIC images at higher annealing temperatures likely originates from local defects or partial delamination, which do not significantly affect the overall EQE spectrum. Hence, the apparent discrepancy between local and area-averaged measurements arises from the difference in spatial resolution rather than any inconsistency in device performance.

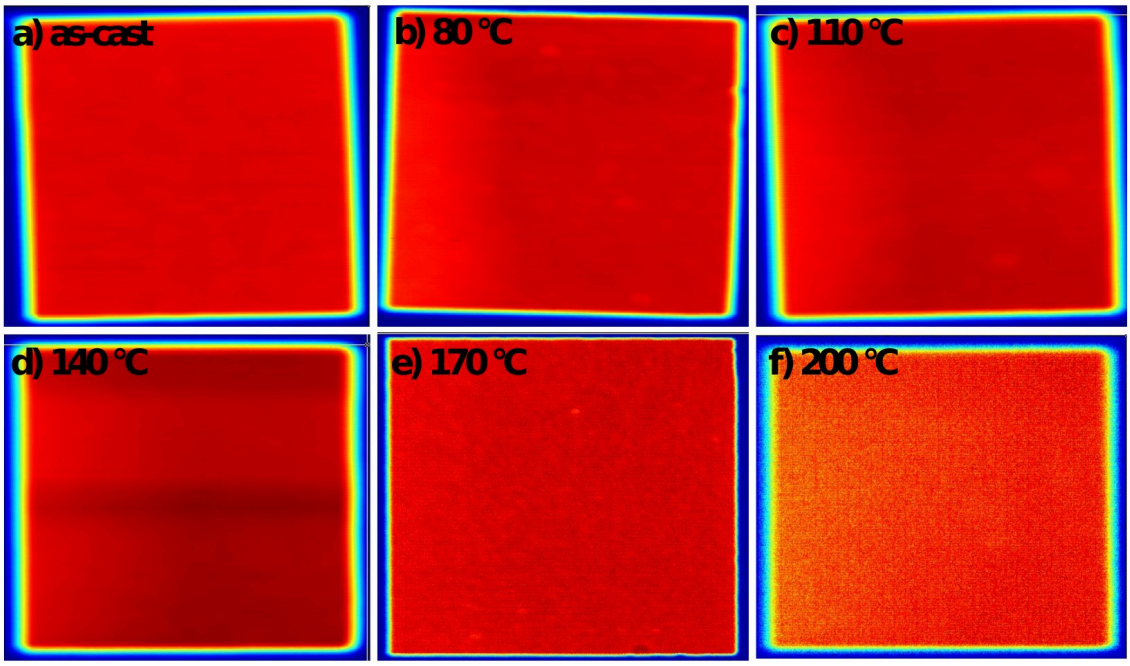

Figure 4: Full-size LBIC scans of the PM6:Y6-based solar cells. The light-beam induced current (LBIC) was measured using a Keithley 2400 and an excitation laser at 658 nm. Each sub-image is a response to the actual cell size of 7 × 6 mm². (a) as-cast, (b) 80 °C, (c) 110 °C, (d) 140 °C, (e) 170 °C, and (f) 200 °C.

All PLI, ELI, and LBIC images in this study were processed using a consistent, normalized color scale applied identically to every sample. This approach enables reliable comparison of spatial variations in recombination and photocurrent distribution, which are the primary quantities of interest for these techniques. Because the analysis focuses on relative spatial contrast rather than absolute signal magnitude, the normalized representation does not influence the interpretation of the thermally induced trends. Importantly, all imaging observations are contextualized with complementary GIWAXS, AFM, and device-level measurements, ensuring that the spatial maps support a coherent and well-correlated picture of morphology-dependent optoelectronic behavior.

2.5. Atomic Force Microscopy (AFM)

Atomic force microscopy (AFM) is utilized to examine the topography of the film surface and to investigate the impact of thermal annealing at different temperatures on the morphology

© 2026 The authors · CC BY 4.0

of the film's photoactive layer. The topographical images of PM6:Y6 blends subjected to thermal annealing at various temperatures are shown in **Figure 5**. No significant changes in topography are observed in the thermally annealed films up to 140 °C. However, thermal annealing at temperatures higher than 170 °C caused the film's surface morphology to change, and crystallization, leading to finer structures, was observed.

The AFM images reveal the emergence of fine fibrillar-like feathers at high annealing temperatures, indicating that the polymer PM6 is getting enriched at the film's surface, which would not be an issue in the case of devices, since the hole extraction takes place at the top of the film, facilitated by the MoO_3 charge extraction layer. However, such vertical stratification is not warranted within devices, since the interaction with MoO_3 may cause the enrichment of that phase, which shows a similar interfacial energy as MoO_3. A non-favorable enrichment of Y6 near the hole extracting the MoO_3 layer could be a reason for the reduction in open-circuit voltage and fill factor, as observed in the IV data. While AFM alone cannot reveal the material composition of these structures, similar fibrillar morphologies have been reported for both donor and acceptor phases in non-fullerene systems[3]. Thus, the observed surface texture likely reflects a combined reorganization of both PM6 and Y6 components, consistent with the enhanced crystallinity observed by GIWAXS (**Figure S7** and **Table S1** in SI) and the associated changes in charge extraction and device performance. Such a crystallization process may cause a rearrangement of the vertical phase distribution, leading to potentially unfavorable material gradients.

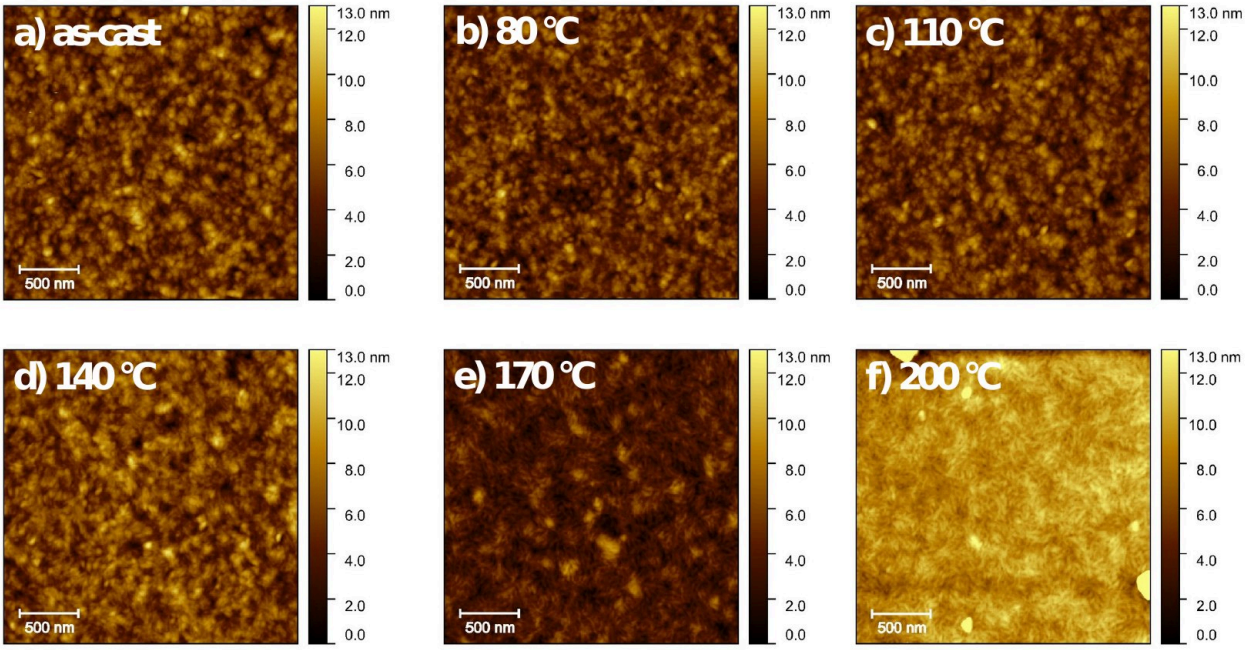

Figure 5: Atomic force microscopy (AFM) of PM6:Y6 layers subjected to different annealing temperatures: (a) as-cast, (b) 80 °C, (c) 110 °C, (d) 140 °C, (e) 170 °C, and (f) 200 °C. The images show the evolution of the surface morphology and increased phase aggregation with higher annealing temperatures. All the images are presented with the same height scale (0-13 nm) for direct comparison.

AFM analysis further reveals a progressive increase in surface roughness and domain size with rising annealing temperature, indicating gradual morphological reorganization within the PM6:Y6 blend. RMS roughness increased from approximately 1.3 nm (as-cast) to 3.2 nm (200 °C), while the characteristic domain spacing expanded from ~30 nm to ~70 nm (**Table S2**). These trends reflect enhanced polymer crystallization and coarsening of the donor–acceptor network at elevated temperatures. The emergence of fibrillar features above 170 °C suggests excessive molecular ordering and vertical phase segregation, consistent with the structural evolution observed in GIWAXS and the accompanying decline in device performance. GIWAXS analysis revealed that PM6:Y6 films maintained a face-on orientation with constant π–π stacking, while moderate annealing at 110 °C enhanced isotropic crystallinity and molecular ordering. In contrast, higher temperatures (≥140 °C) increased face-on crystallinity but led to excessive phase separation, resulting in reduced device performance. The addition of 1D line-cut (**Figure S8**) profiles and extracted coherence length and π–π stacking distances provides a clearer understanding of how thermal annealing modulates lamellar packing and crystalline coherence, and how these changes relate to the trends observed in PLI, ELI, and AFM measurements.

High-resolution scanning electron microscopy (SEM) measurements are conducted to examine the cross-sections of the thin films, as seen in **Figure S9**. The cast films appear thicker than other annealed samples, possibly due to residual solvent impeding the formation of an ideal film. Thermal annealing at elevated temperatures (140 °C and above) induces morphological alterations, evidenced by a somewhat increased contrast. At higher temperatures and upon closer inspection, a brighter layer appears to be at the top of the films, indicating and confirming the enrichment of the polymer PM6 near the surface of the films. However, as stated before, the vertical stratification can differ for complete solar cell layer stacks. Raman spectra (**Figure S10**) reveal the onset of structural disorders above 170 °C, consistent with the irreversible morphological and electronic degradation deduced from the optical measurements. Although detailed peak fitting was not performed, the irreversible broadening and intensity decrease of the C=C stretching vibration (~1510 cm^{-1})

© 2026 The authors · CC BY 4.0

after high-temperature treatment are consistent with structural disorder in conjugated polymers, confirming irreversible morphological changes within the PM6:Y6 films.

While all devices share identical ETL/HTL processing, and the temperature-dependent trends correlate directly with GIWAXS, AFM, PLI, and ELI signatures of bulk morphological evolution, some degree of interfacial degradation cannot be entirely ruled out. In our previous work on thermally induced degradation in PM6:Y6 devices, we demonstrated that high-temperature treatment can modify interfacial energetics and enhance non-radiative recombination pathways[40]. Nevertheless, the gradual and morphology-correlated changes observed here indicate that bulk active-layer reorganization is the dominant factor governing device behavior as a function of annealing temperature.

CONCLUSION

This study, which leverages multiple optical and optoelectronic imaging techniques, provides insight into the impact of thermal degradation on state-of-the-art PM6:Y6 devices. However, aside from the pattern caused by the use of chloroform for coating the photoactive layer and a few defects within the charge transport or electrode layers, the devices remain homogeneous across the photoactive area. While only minor variations in device efficiency are observed up to 140 °C, more substantial reductions in Voc and FF values occur at higher annealing temperatures. Although a quantitative analysis of phase-region purity and domain size (e.g., by RSoXS) could further substantiate the morphological evolution, in conjunction with the tendency of PM6 to crystallize, as observed in the AFM and SEM images, vertical phase separation / stratification different from that of pristine films can occur in complete device stacks. This finding indicates that charge transport and extraction are affected by structural and nanoscale morphological alterations. A reduced radiative exciton recombination, as observed in photoluminescence and electroluminescence imaging results, appears to indicate reduced component demixing, which may hinder charge percolation. Additional degradation mechanisms can arise due to changes within the charge transport layer itself, specifically within the MoO_3 layer. Furthermore, photoluminescence and electroluminescence studies reveal that moderate annealing improves exciton dissociation, while excessive heating enhances non-radiative recombination. Complementary Raman spectroscopy experiments further confirmed these observations by demonstrating that high-temperature treatment induces irreversible structural disorder, which correlates with the increased non-radiative recombination observed in the optical measurements. Taken together, the structural evolution revealed by GIWAXS and AFM, alongside the simultaneous decrease in PL/EL emission and V_{OC}, consistently indicates that thermal annealing induces crystallization-driven phase separation, which enhances non-radiative recombination and energy losses, ultimately leading to performance degradation in state-of-the-art PM6:Y6 solar cells.

Associated Content

Supporting Information

Dark J–V characteristics of devices, statistical evaluation of device performance, steady-state photoluminescence spectra (overlaid and individual), electroluminescence spectra (overlaid and individual), 2D GIWAXS patterns, OOP/IP line cuts, and azimuthal orientation analysis, crystallite size and stacking distance evolution, AFM height images and morphological parameters, SEM cross-sectional morphology, Raman spectroscopy during heating/cooling cycles, light J–V characteristics comparing pre- and post-electrode annealing.

EXPERIMENTAL SECTION

Sample preparation

All the thin films were prepared on quartz glass in order to perform the optical measurements. In contrast, thin films for electrochemical measurements were processed on ITO/ZnO substrates. Thin films for structural and morphological characterization were coated on either Si or glass substrates using the same parameters as those for the active layer of the solar cell devices.

Inverted BHJ solar cells were fabricated with a device configuration of ITO/ZnO/PM6:Y6/MoO_3/Ag. Glass substrates with pre-patterned indium tin oxide (ITO, 16 Ω sq^{-1}) were first cleaned with the dilute detergent solution for 20 min in an ultrasonic bath. Samples were rinsed in flowing deionized water for 5 minutes, followed by a sequential bath of acetone and isopropanol for 15 minutes each. In the next step, these cleaned samples were exposed to UV-ozone plasma cleaning for 15 min. A thin layer of ZnO is spin-coated (4000 rpm) using the ZnO precursor solution. The films were baked at 150 °C for 15 min in the air to give the film a thickness of 30 to 35 nm. The ZnO films were transferred into the glovebox for active layer deposition. The photoactive layer solutions were prepared a day before deposition using polymer PM6 (purchased from 1-material) as the donor mix with Y6 as the acceptor (purchased from Organtec Ltd-BETTERCHEM). The donor and acceptors were dissolved in chloroform (CF) at a ratio of 1:1.2 (wt.%), with an overall concentration of 15.11 mg/mL, and stirred overnight at a temperature of 40 °C. As a solvent additive, 0.5 vol.% chloro-naphthalene (CN) was added to the host solution. The active layers were spin-coated over the ZnO-coated substrates at 2500 rpm to provide a film thickness of ≈90 nm. Afterward, the films were transferred to a thermal evaporator for the evaporation of a 10 nm thick film of MoO_3, followed by a 100 nm thick Ag top electrode with deposition rates of 0.25 and 0.5 Å/s, respectively, through a shadow mask, yielding active areas of 0.42 cm^2 in each device.

Sample Characterizations

Electrical characterization: J–V measurements of solar cells were performed in the glovebox with a Keithley 2400 source meter, and an Oriel Sol3A Class AAA solar simulator calibrated to one sun, AM1.5 G, with a KG-5 silicon reference cell certified by Newport. The EQE measurements were performed at zero bias by illuminating the device with a monochromatic light supplied by a Xenon arc lamp in combination with a dual-grating monochromator.

Grazing Incidence Wide Angle X-ray Scattering (GIWAXS): The GIWAXS measurements were carried out with a SAXSLAB laboratory instrument using a CuKα X-ray source (8.05 keV, 1.54 Å) and a Pilatus 300 K detector. The incident angle was 0.2°, and the sample-to-detector distance (SDD) was set to 95 mm. The transformation to q-space, radial cuts for the in-plane /out-of-plane analysis, and azimuthal cuts for orientation analysis were processed by the MATLAB-based package GIXSGUI.

Atomic Force Microscope (AFM): Film topography was characterized using a Veeco/Bruker Dimension atomic force microscope in tapping mode to gain further insight into possible morphology changes with super sharp tips (TESP-SS). The images

© 2026 The authors · CC BY 4.0

were analyzed primarily by Nanoscope v720 software during the measurements and by Gwyddion, a multiplatform, modular, free software.

ELI: The Keithley 2400 Source Measurement Unit (SMU) supports a constant current of 20 mA for the device under measurement. A Si CCD camera, specifically the ANDOR iKon-M, is positioned above the device and used to capture the optical signal produced by the device under the applied current. The camera is cooled to -50 °C prior to the measurement. The captured signals are then processed and visualized using software. All measurements are conducted in a dark environment at room temperature.

PLI: In the dark environment and room temperature, LED components powered by EA-PS 2042-06 B serve as the radiation devices. Above these devices, a Si CCD camera (ANDOR iKon-M) cooled to -50 °C captures the light signals generated when the devices are irradiated by a laser (470 nm), forming visual images in the software.

LBIC: The Laser Beam Induced Current (LBIC) technique relies on the use of a Keithley 2400 instrument to measure the local current generated by a solar cell under the illumination of a 658 nm laser (Insaneware, Germany). The laser is moved point by point (15 um) across the entire cell in a dark environment at room temperature, and the resulting current distribution is recorded and displayed as a scanned map on the computer.

Vapor phase infiltration: The VPI process was conducted in a Veeco Savannah S200 system. The Samples were exposed to 50 alternating cycles of DEZ and H2O at 100°C. During each cycle, the samples were exposed to a DEZ pulse for 300 s, followed by a purge process of 150 s. After the DEZ pulses, the samples were exposed to a single H2O pulse, followed by a purge process of 300 s. The VPI process conditions were carefully adjusted to reduce any morphology changes during the process.

High-resolution scanning electron microscopy: Cross sections of the thin films were obtained by immersing the samples in liquid nitrogen and then cleaving them, resulting in sharp cross-section samples. HRSEM micrographs were taken using a Zeiss Ultra- Plus FEG-SEM operated at 1.5 kV accelerating voltage with a working distance of ~2.7 mm. Backscattered electrons signal (ESB detector) and secondary electrons signal (Inlens detector) were collected simultaneously.

Photoluminescence (PL) spectroscopy: A fiber spectrometer manufactured by Avantes called the AvaSpec ULS-204864 was utilized in order to record PL intensities. For optical excitation, a straightforward laser diode equipped with a wavelength of 405 nm was used.

Electroluminescence (EL) spectroscopy: Solar cells were additionally analyzed using EL spectroscopy across a spectrum of 330–1170 nm. The electroluminescence spectrum of the solar cells was measured in a dark chamber by applying a continuous forward current of 50 mA using a Keithley 2400 SMU, resulting in a current density of 120 mA cm^2. The emitted light was gathered and conveyed through a fiber optic to a silicon spectrometer. The Avantes spectrometer, AvaSpec ULS2048-64, and the OEM software were used to capture the signal over an integration period of 10 seconds with double averaging.

Raman Spectroscopy: Using a backscattering objective, the Raman spectra were obtained at 532 and 633 nm excitation using a WITec alpha300 apryon confocal Raman microscope. The measured Raman spectra were analyzed, and the background subtraction was carried out using the WITec Project FIVE software. The laser's power was adjusted to 0.04 mW for excitation at 532 and 633 nm. The acquisition duration was 25 s, and the average was 10 times for the single spectra.

ACKNOWLEDGMENTS

This work was supported by the King Abdullah University of Science and Technology (KAUST) Office of Sponsored Research (OSR) under Award No. OSR-2018-CARF/CCF-3079. P.M.-B. acknowledges financial support from Deutsche Forschungsgemeinschaft (DFG, German Research Foundation) under Germany's Excellence Strategy—EXC 2089/1—390776260 (e-conversion) and from TUM.solar in the context of the Bavarian Collaborative Research Project Solar Technologies Go Hybrid (SolTech).

AUTHOR INFORMATION

Corresponding Authors

pudo mia — pudomia@yopmail.com

Authors

pudo mia*

Just test

REFERENCES

(1) Sun, R.; Wu, Y.; Yang, X.; Gao, Y.; Chen, Z.; Li, K.; Qiao, J.; Wang, T.; Guo, J.; Liu, C. Single-Junction Organic Solar Cells with 19.17% Efficiency Enabled by Introducing One Asymmetric Guest Acceptor. Adv. Mater. 2022, 34, 2110147.

(2) Han, C.; Wang, J.; Zhang, S.; Chen, L.; Bi, F.; Wang, J.; Yang, C.; Wang, P.; Li, Y.; Bao, X. Over 19% Efficiency Organic Solar Cells by Regulating Multidimensional Intermolecular Interactions. Adv. Mater. 2023, 35, 2208986.

(3) Zhu, L.; Zhang, M.; Xu, J.; Li, C.; Yan, J.; Zhou, G.; Zhong, W.; Hao, T.; Song, J.; Xue, X. Single-Junction Organic Solar Cells with over 19% Efficiency Enabled by a Refined Double-Fibril Network Morphology. Nat. Mater. 2022, 21, 656–663.

(4) Wei, Y.; Chen, Z.; Lu, G.; Yu, N.; Li, C.; Gao, J.; Gu, X.; Hao, X.; Lu, G.; Tang, Z. Binary Organic Solar Cells Breaking 19% via Manipulating the Vertical Component Distribution. Adv. Mater. 2022, 34, 2204718.

(5) Luo, S.; Li, C.; Zhang, J.; Zou, X.; Zhao, H.; Ding, K.; Huang, H.; Song, J.; Yi, J.; Yu, H. Auxiliary Sequential Deposition Enables 19%-Efficiency Organic Solar Cells Processed from Halogen-Free Solvents. Nat. Commun. 2023, 14, 6964.

(6) Gao, W.; Qi, F.; Peng, Z.; Lin, F. R.; Jiang, K.; Zhong, C.; Kaminsky, W.; Guan, Z.; Lee, C. S.; Marks, T. J. Achieving 19% Power Conversion Efficiency in Planar-Mixed Heterojunction Organic Solar Cells Using a Pseudosymmetric Electron Acceptor. Adv. Mater. 2022, 34, 2202089.

(7) Li, D.; Deng, N.; Fu, Y.; Guo, C.; Zhou, B.; Wang, L.; Zhou, J.; Liu, D.; Li, W.; Wang, K. Fibrillization of Non-Fullerene Acceptors Enables 19% Efficiency Pseudo-Bulk Heterojunction Organic Solar Cells. Adv. Mater. 2023, 35, 2208211.

(8) Yao, Z.; Cao, X.; Bi, X.; He, T.; Li, Y.; Jia, X.; Liang, H.; Guo, Y.; Long, G.; Kan, B. Complete Peripheral Fluorination of the Small-Molecule Acceptor in Organic Solar Cells Yields Efficiency over 19%. Angew. Chem., Int. Ed. 2023, 62, e202312630.

(9) Li, Y.; Xu, G.; Cui, C.; Li, Y. Flexible and Semitransparent Organic Solar Cells. Adv. Energy Mater. 2018, 8, 1701791.

(10) Bergqvist, J.; Österberg, T.; Melianas, A.; Ever Aguirre, L.; Tang, Z.; Cai, W.; Ma, Z.; Kemerink, M.; Gedefaw, D.; Andersson, M. R. Asymmetric Photocurrent Extraction in Semitransparent Laminated Flexible Organic Solar Cells. npj Flexible Electron. 2018, 2, 1–8.

(11) Shin, D. H.; Jang, C. W.; Lee, H. S.; Seo, S. W.; Choi, S.-H. Semitransparent Flexible Organic Solar Cells Employing Doped-Graphene Layers as Anode and Cathode Electrodes. ACS Appl. Mater. Interfaces 2018, 10, 3596–3601.

© 2026 The authors · CC BY 4.0

(12) Angmo, D.; Hösel, M.; Krebs, F. C. All Solution Processing of ITO-Free Organic Solar Cell Modules Directly on Barrier Foil. Sol. Energy Mater. Sol. Cells 2012, 107, 329–336.

(13) Pan, W.; Han, Y.; Wang, Z.; Luo, Q.; Ma, C.; Ding, L. Over 1 cm² Flexible Organic Solar Cells. J. Semicond. 2021, 42, 050301.

(14) Wang, Y.; Wang, G.; Xing, Y.; Adil, M. A.; Memon, W. A.; Chang, Y.; Liu, L.; Yang, C.; Zhang, M.; Li, D. Top and Bottom Electrode Optimization Enabled High-Performance Flexible and Semi-Transparent Organic Solar Cells. Mater. Chem. Front. 2021, 5, 4310–4316.

(15) Su, Y.-W.; Lan, S.-C.; Wei, K.-H. Organic Photovoltaics. Mater. Today 2012, 15, 554–562.

(16) Wang, H. C.; Cheng, P.; Tan, S.; Chen, C. H.; Chang, B.; Tsao, C. S.; Chen, L. Y.; Hsieh, C. A.; Lin, Y. C.; Cheng, H. W. Sequential Deposition of Donor and Acceptor Provides High-Performance Semitransparent Organic Photovoltaics Having a Pseudo p–i–n Active Layer Structure. Adv. Energy Mater. 2021, 11, 2003576.

(17) Po, R.; Bernardi, A.; Calabrese, A.; Carbonera, C.; Corso, G.; Pellegrino, A. From Lab to Fab: How Must the Polymer Solar Cell Materials Design Change? An Industrial Perspective. Energy Environ. Sci. 2014, 7, 925–943.

(18) Krebs, F. C.; Fyenbo, J.; Jørgensen, M. Product Integration of Compact Roll-to-Roll Processed Polymer Solar Cell Modules: Methods and Manufacture Using Flexographic Printing, Slot-Die Coating and Rotary Screen Printing. J. Mater. Chem. 2010, 20, 8994–9001.

(19) Riede, M.; Spoltore, D.; Leo, K. Organic Solar Cells—The Path to Commercial Success. Adv. Energy Mater. 2021, 11, 2002653.

(20) Wu, J.; Gao, M.; Chai, Y.; Liu, P.; Zhang, B.; Liu, J.; Ye, L. Towards a Bright Future: The Versatile Applications of Organic Solar Cells. Mater. Rep.: Energy 2021, 1, 100062.

(21) Xue, R.; Zhang, J.; Li, Y.; Li, Y. Organic Solar Cell Materials toward Commercialization. Small 2018, 14, 1801793.

(22) Synooka, O.; Eberhardt, K. R.; Singh, C. R.; Hermann, F.; Ecke, G.; Ecker, B.; von Hauff, E.; Gobsch, G.; Hoppe, H. Influence of Thermal Annealing on PCDTBT:PCBM Composition Profiles. Adv. Energy Mater. 2014, 4, 1300981.

(23) Yang, W.; Wang, W.; Wang, Y.; Sun, R.; Guo, J.; Li, H.; Shi, M.; Guo, J.; Wu, Y.; Wang, T. Balancing the Efficiency, Stability, and Cost Potential for Organic Solar Cells via a New Figure of Merit. Joule 2021, 5, 1209–1230.

(24) Seemann, A.; Sauermann, T.; Lungenschmied, C.; Armbruster, O.; Bauer, S.; Egelhaaf, H.-J.; Hauch, J. Reversible and Irreversible Degradation of Organic Solar Cell Performance by Oxygen. Sol. Energy 2011, 85, 1238–1249.

(25) Yang, W.; Yao, Y.; Wu, C.-Q. Mechanisms of Device Degradation in Organic Solar Cells: Influence of Charge Injection at the Metal/Organic Contacts. Org. Electron. 2013, 14, 1992–2000.

(26) Glen, T. S.; Scarratt, N. W.; Yi, H.; Iraqi, A.; Wang, T.; Kingsley, J.; Buckley, A. R.; Lidzey, D. G.; Donald, A. M. Dependence on Material Choice of Degradation of Organic Solar Cells Following Exposure to Humid Air. J. Polym. Sci., Part B: Polym. Phys. 2016, 54, 216–224.

(27) Song, Q.; Wang, M.; Obbard, E.; Sun, X.; Ding, X.; Hou, X.; Li, C. Degradation of Small-Molecule Organic Solar Cells. Appl. Phys. Lett. 2006, 89, 251118.

(28) Turkovic, V.; Engmann, S.; Egbe, D. A.; Himmerlich, M.; Krischok, S.; Gobsch, G.; Hoppe, H. Multiple Stress Degradation Analysis of the Active Layer in Organic Photovoltaics. Sol. Energy Mater. Sol. Cells 2014, 120, 654–668.

(29) Alam, S.; Islam, M. M.; Chowdhury, S.; Meitzner, R.; Kästner, C.; Schubert, U. S.; Hoppe, H. Disentanglement of Degradation Mechanisms by Analyzing Aging Dynamics of Environmentally Friendly Processed Polymer Solar Cells. Energy Technol. 2020, 8, 2000116.

(30) Greenbank, W.; Hirsch, L.; Wantz, G.; Chambon, S. Interfacial Thermal Degradation in Inverted Organic Solar Cells. Appl. Phys. Lett. 2015, 107, 263301.

(31) Seeland, M.; Roesch, R.; Hoppe, H. Luminescence Imaging of Polymer Solar Cells: Visualization of Progressing Degradation. J. Appl. Phys. 2011, 109, 063106.

(32) Rösch, R.; Tanenbaum, D. M.; Jørgensen, M.; Seeland, M.; Bärenklau, M.; Hermenau, M.; Voroshazi, E.; Lloyd, M. T.; Galagan, Y.; Zimmermann, B.; Würfel, U.; Hösel, M.; Dam, H. F.; Gevorgyan, S. A.; Kudret, S.; Maes, W.; Lutsen, L.; Vanderzande, D.; Andriessen, R.; Teran-Escobar, G.; Lira-Cantu, M.; Rivaton, A.; Uzunoğlu, G. Y.; Germack, D.; Andreasen, B.; Madsen, M. V.; Norrman, K.; Hoppe, H.; Krebs, F. C. Investigation of the Degradation Mechanisms of a Variety of Organic Photovoltaic Devices by Combination of Imaging Techniques—the ISOS-3 Inter-Laboratory Collaboration. Energy Environ. Sci. 2012, 5, 6521–6540.

(33) Rösch, R.; Eberhardt, K.-R.; Engmann, S.; Gobsch, G.; Hoppe, H. Polymer Solar Cells with Enhanced Lifetime by Improved Electrode Stability and Sealing. Sol. Energy Mater. Sol. Cells 2013, 117, 59–66.

(34) Jørgensen, M.; Norrman, K.; Krebs, F. C. Stability/Degradation of Polymer Solar Cells. Sol. Energy Mater. Sol. Cells 2008, 92, 686–714.

(35) Wang, Z.; Peng, Z.; Xiao, Z.; Seyitliyev, D.; Gundogdu, K.; Ding, L.; Ade, H. Thermodynamic Properties and Molecular Packing Explain Performance and Processing Procedures of Three D18:NFA Organic Solar Cells. Adv. Mater. 2020, 32, 2005386.

(36) Agresti, A.; Pescetelli, S.; Busby, Y.; Aernouts, T. Thermally Induced Fullerene Domain Coarsening Process in Organic Solar Cells. IEEE Trans. Electron Devices 2019, 66, 678–688.

(37) Li, Z.; Chiu, K. H.; Ashraf, R. S.; Fearn, S.; Dattani, R.; Wong, H. C.; Tan, C.-H.; Wu, J.; Cabral, J. T.; Durrant, J. R. Toward Improved Lifetimes of Organic Solar Cells under Thermal Stress: Substrate-Dependent Morphological Stability of PCDTBT:PCBM Films and Devices. Sci. Rep. 2015, 5, 1–9.

(38) Conings, B.; Bertho, S.; Vandewal, K.; Senes, A.; D'Haen, J.; Manca, J.; Janssen, R. A. Modeling the Temperature-Induced Degradation Kinetics of the Short-Circuit Current in Organic Bulk Heterojunction Solar Cells. Appl. Phys. Lett. 2010, 96, 163301.

(39) Alam, S.; Gavrik, A.; Meitzner, R.; Hoeppener, S.; Dyakonov, V.; Baumann, A.; Schubert, U. S.; Hoppe, H. Thermally Induced Degradation of PBDTTT-CT:PCBM-Based Polymer Solar Cells. J. Phys. D: Appl. Phys. 2019, 52, 475501.

(40) Alam, S.; Aldosari, H.; Petoukhoff, C. E.; Váry, T.; Althobaiti, W.; Alqurashi, M.; Tang, H.; Khan, J. I.; Nádaždy, V.; Müller-Buschbaum, P. Thermally Induced Degradation in PM6:Y6-Based Bulk Heterojunction Organic Solar Cells. Adv. Funct. Mater. 2024, 34, 2308076.

(41) Duan, L.; Zhang, Y.; He, M.; Deng, R.; Yi, H.; Wei, Q.; Zou, Y.; Uddin, A. Burn-In Degradation Mechanism Identified for Small Molecular Acceptor-Based High-Efficiency Nonfullerene Organic Solar Cells. ACS Appl. Mater. Interfaces 2020, 12, 27433–27442.

(42) Zhao, Y.; Wu, Z.; Liu, X.; Zhong, Z.; Zhu, R.; Yu, J. Revealing the Photo-Degradation Mechanism of PM6:Y6-Based High-Efficiency Organic Solar Cells. J. Mater. Chem. C 2021, 9, 13972–13980.

(43) Meitzner, R.; Faber, T.; Alam, S.; Amand, A.; Rösch, R.; Büttner, M.; Herrmann-Westendorf, F.; Presselt, M.; Ciammaruchi, L.; Visoly-Fisher, I. Impact of P3HT Materials Properties and Layer Architecture on OPV Device Stability. Sol. Energy Mater. Sol. Cells 2019, 202, 110151.

(44) Alam, S.; Islam, M. M.; Meitzner, R.; Hager, M.; Schubert, U. S.; Laquai, F.; Hoppe, H.; Zou, Y. Aging of Quinoxaline-Based Polymer Solar Cells under UV-Free White Light. Sustainable Energy Fuels 2024, 8, 535–545.

(45) Alam, S.; Nádaždy, V.; Váry, T.; Friebe, C.; Meitzner, R.; Ahner, J.; Anand, A.; Karuthedath, S.; De Castro, C. S. P.; Göhler, C.; Dietz, S.; Cann, J.; Kästner, C.; Konkin, A.; Beenken, W.; Anton, A. M.; Ulbricht, C.; Sperlich, A.; Hager, M. D.; Ritter, U.; Kremer, F.; Brüggemann, O.; Schubert, U. S.; Egbe, D. A. M.; Welch, G. C.; Dyakonov, V.; Deibel, C.; Laquai, F.; Hoppe, H. Uphill and Downhill Charge Generation from Charge Transfer to Charge Separated States in Organic Solar Cells. J. Mater. Chem. C 2021, 9, 14463–14489.

(46) Alam, S.; Petoukhoff, C. E.; Jurado, J. P.; Aldosari, H.; Jiang, X.; Váry, T.; Al Nasser, H.; Dahman, A.; Althobaiti, W.; Lopez, S. P. G. Influence of Thermal Annealing on Microstructure, Energetic Landscape and Device Performance of P3HT:PCBM-Based Organic Solar Cells. J. Phys. Energy 2024, 6, 025013.

(47) Hoppe, H.; Sariciftci, N. S. Morphology of Polymer/Fullerene Bulk Heterojunction Solar Cells. J. Mater. Chem. 2006, 16, 45–61.

(48) Schaffer, C. J.; Palumbiny, C. M.; Niedermeier, M. A.; Jendrzejewski, C.; Santoro, G.; Roth, S. V.; Müller-Buschbaum, P. Direct Evidence of Morphological Degradation on a Nanometer Scale in Polymer Solar Cells. Adv. Mater. 2013, 25, 6760–6764.

(49) Heinrich, D.; Hufnagel, M.; Singh, C. R.; Fischer, M.; Alam, S.; Hoppe, H.; Thurn-Albrecht, T.; Thelakkat, M. Nanoscale Morphology from Donor–Acceptor Block Copolymers: Formation and Functions. Adv. Polym. Sci. 2017, 272, 157–191.

(50) Tan, L.; Yang, F.; Kim, M. R.; Li, P.; Gangadharan, D. T.; Margot, J.; Izquierdo, R.; Chaker, M.; Ma, D. Enhanced Long-Term and Thermal Stability of Polymer Solar Cells in Air at High Humidity with the Formation of Unusual Quantum Dot Networks. ACS Appl. Mater. Interfaces 2017, 9, 26257–26267.

(51) Duan, L.; Guli, M.; Zhang, Y.; Yi, H.; Haque, F.; Uddin, A. The Air Effect in the Burn-In Thermal Degradation of Nonfullerene Organic Solar Cells. Energy Technol. 2020, 8, 1901401.

© 2026 The authors · CC BY 4.0

(52) Wang, Y.; Lee, J.; Hou, X.; Labanti, C.; Yan, J.; Mazzolini, E.; Parhar, A.; Nelson, J.; Kim, J. S.; Li, Z. Recent Progress and Challenges toward Highly Stable Nonfullerene Acceptor-Based Organic Solar Cells. Adv. Energy Mater. 2021, 11, 2003002.

(53) Cha, H.; Wu, J. Understanding What Determines the Organic Solar Cell Stability. Joule 2021, 5, 1322–1325.

(54) Li, Y.; Li, T.; Lin, Y. Stability: Next Focus in Organic Solar Cells Based on Non-Fullerene Acceptors. Mater. Chem. Front. 2021, 5, 2907–2930.

(55) Cho, H. W.; An, N. G.; Park, S. Y.; Shin, Y. S.; Lee, W.; Kim, J. Y.; Song, S. Thermally Durable Nonfullerene Acceptor with Nonplanar Conjugated Backbone for High-Performance Organic Solar Cells. Adv. Energy Mater. 2020, 10, 1903585.

(56) Alam, S.; Meitzner, R.; Kaestner, C.; Ulbricht, C.; Hoeppener, S.; Egbe, D. A. M.; Schubert, U. S.; Hoppe, H. Controlling Donor Crystallinity and Phase Separation in Bulk Heterojunction Solar Cells by the Introduction of Orthogonal Solvent Additives. MRS Adv. 2018, 3, 1891–1900.

(57) Kim, T.; Choi, J.; Kim, H. J.; Lee, W.; Kim, B. J. Comparative Study of Thermal Stability, Morphology, and Performance of All-Polymer, Fullerene–Polymer, and Ternary Blend Solar Cells Based on the Same Polymer Donor. Macromolecules 2017, 50, 6861–6871.

(58) Ma, W.; Yang, C.; Gong, X.; Lee, K.; Heeger, A. J. Thermally Stable, Efficient Polymer Solar Cells with Nanoscale Control of the Interpenetrating Network Morphology. Adv. Funct. Mater. 2005, 15, 1617–1622.

(59) Du, X.; Heumueller, T.; Gruber, W.; Almora, O.; Classen, A.; Qu, J.; He, F.; Unruh, T.; Li, N.; Brabec, C. J. Unraveling the Microstructure-Related Device Stability for Polymer Solar Cells Based on Nonfullerene Small-Molecular Acceptors. Adv. Mater. 2020, 32, 1908305.

(60) Kastner, C.; Xuechen, J.; Egbe, D. A. M.; Ade, H.; Hoppe, H. Correlating Domain Purity with Charge Carrier Mobility in Bulk Heterojunction Polymer Solar Cells. Proc. SPIE 2014, 9184, 91840Z.

(61) Hoppe, H.; Niggemann, M.; Winder, C.; Kraut, J.; Hiesgen, R.; Hinsch, A.; Meissner, D.; Sariciftci, N. S. Nanoscale Morphology of Conjugated Polymer/Fullerene-Based Bulk-Heterojunction Solar Cells. Adv. Funct. Mater. 2004, 14, 1005–1011.

(62) Nguyen, L. H.; Hoppe, H.; Erb, T.; Gunes, S.; Gobsch, G.; Sariciftci, N. S. Effects of Annealing on the Nanomorphology and Performance of Poly(alkylthiophene):Fullerene Bulk-Heterojunction Solar Cells. Adv. Funct. Mater. 2007, 17, 1071–1078.

(63) Harillo-Baños, A.; Rodríguez-Martínez, X.; Campoy-Quiles, M. Efficient Exploration of the Composition Space in Ternary Organic Solar Cells by Combining High-Throughput Material Libraries and Hyperspectral Imaging. Adv. Energy Mater. 2020, 10, 1902417.

(64) Reinhardt, J.; Apilo, P.; Zimmermann, B.; Rousu, S.; Würfel, U. Determining the Photocurrent of Individual Cells within an Organic Solar Module by LBIC and the Filtering Approach: Experiments and Simulations. Sol. Energy Mater. Sol. Cells 2015, 134, 157–164.

(65) Rodríguez-Martínez, X.; Sánchez-Díaz, A.; Liu, G.; Niño, M.; Cabanillas-Gonzalez, J.; Campoy-Quiles, M. Combinatorial Optimization of Evaporated Bilayer Small Molecule Organic Solar Cells through Orthogonal Thickness Gradients. Org. Electron. 2018, 59, 288–292.

(66) Xu, Z.; Madalaimuthu, J. P.; Slowik, J. B.; Meitzner, R.; Anand, A.; Alam, S.; Corte, H.; Stumpf, S.; Schubert, U. S.; Hoppe, H. Compatible Solution-Processed Interface Materials for Improved Efficiency of Polymer Solar Cells. Adv. Mater. Interfaces 2023, 10, 2201740.

(67) Rau, U. Reciprocity Relation between Photovoltaic Quantum Efficiency and Electroluminescent Emission of Solar Cells. Phys. Rev. B 2007, 76, 085303.

(68) Xin, J.; Zhao, C.; Geng, Z.; Xue, W.; Chen, Z.; Song, C.; Yan, H.; Liang, Q.; Miao, Z.; Ma, W. Elucidating the Thermal Degradation Mechanism of Y6-Based Organic Solar Cells by Establishing Structure–Property Correlation. Adv. Energy Mater. 2024, 14, 2401433.

(69) Gaponenko, M. S.; Lutich, A. A.; Tolstik, N. A.; Onushchenko, A. A.; Malyarevich, A. M.; Petrov, E. P.; Yumashev, K. V. Temperature-Dependent Photoluminescence of PbS Quantum Dots in Glass: Evidence of Exciton State Splitting and Carrier Trapping. Phys. Rev. B 2010, 82, 125320.

(70) Duan, L.; Zhang, Y.; Yi, H.; Haque, F.; Xu, C.; Wang, S.; Uddin, A. Thermal Annealing Dependent Dielectric Properties and Energetic Disorder in PffBT4T-2OD-Based Organic Solar Cells. Mater. Sci. Semicond. Process. 2020, 105, 104750.

© 2026 The authors. Published in *Solar Cell Insights (Dev)* under the CC BY 4.0 licence.